Optical Spectroscopy for Characterization of Metal Oxide Nanofibers

16

Roman Viter and Igor Iatsunskyi

Contents

Introduction 524
Raman Spectroscopy 524
Fundamentals of Raman Spectroscopy 524
Raman Techniques and Experimental Setups 526
Raman Spectroscopy of Metal Oxide Nanofibers 527
Fourier Transform Infrared (FTIR) Spectroscopy 531
Fundamentals of FTIR Spectroscopy 531
FTIR Spectrometers and Measuring Principals 533
FTIR Spectroscopy of Metal Oxide Nanofibers 534
UV-Visible Optical Spectroscopy for Investigation of Metal Oxide Nanofibers 535
Main Fundamental Optical Parameters of Metal Oxide Nanostructures 535
Diffuse Reflectance Spectroscopy for Characterization of Metal Oxide Nanofibers 537
Photoluminescence Spectroscopy for Characterization of Metal Oxide Nanofibers 542
Photoluminescence of Core-Shell and Hollow Metal Oxide Nanofibers 550
Correlation Between Structural, Electronic, and Optical Properties of Metal Oxide Nanofibers 552
Optical and Optoelectronic Applications of Metal Oxide Nanofibers 552
Conclusions and Future Prospects 553
References 553

Abstract

Optical spectroscopy methods are powerful nondestructive analytical methods for investigating electronic and optical properties of materials. Due to unique properties of metal oxide nanofibers, optical methods can provide important information about fundamental properties of metal oxide nanofibers, influence of structural

R. Viter (✉)
Institute of Atomic Physics and Spectroscopy, University of Latvia, Riga, Latvia

I. Iatsunskyi
NanoBioMedical Centre, Adam Mickiewicz University, Poznan, Poland

© Springer Nature Switzerland AG 2019

A. Barhoum et al. (eds.), *Handbook of Nanofibers*,
https://doi.org/10.1007/978-3-319-53655-2_10

properties to the optical and electronic ones, and applications of metal oxide nanofibers. Optical methods involve different techniques, using light from UV-Vis-IR regions and involving different parts of the materials (free electrons, ions, etc.) into interaction with light.

This chapter is dedicated to the characterization of metal oxide nanofibers using diffuse reflectance, photoluminescence, and Raman and Fourier transform infrared (FTIR) spectroscopy. General principles of these methods will be described. Calculation of the main fundamental parameters (band gap, defect levels, emission bands, etc.) will be discussed. Influence of structure parameters (such as nanofibers dimensions, chemical composition, dopants, etc.) on optical properties of metal oxide nanostructures will be demonstrated. Possible perspectives of applications of metal oxide nanofibers in optical devices will be shown.

Keywords
Metal oxide nanofibers · FTIR · Raman · Optical spectroscopy · Photoluminescence spectroscopy

Introduction

All nanostructured solids demonstrate a significant interaction with light, which involves electronic and ionic contributions and depends on the spectral region of the light.

Comparing with different types of nanostructures, 1D nanostructures are confined along the XY plane. Their periodic structure has a long order of periodicity only along the Z axis. Due to high surface-to-volume aspect ratio, a number of surface defects in 1D nanostructures, influencing the fundamental properties of the nanostructures, are expected.

Metal oxides are well-known semiconductor and dielectric materials. Metal oxides have bound electrons, located in the valence band, which can make a transition to the conductance band (free electrons). The energetic distance between the valence band (VB) and conductance band (CB), called a band gap, is in the range of 2–6 eV for metal oxides. Due to structural defects, new energetic states could appear into the band gap of metal oxides, affecting structural, electronic, and optical properties.

Optical methods are nondestructive and precise techniques, which allow to investigate optical properties of solids. In this chapter, methods of analysis of optical properties of 1D metal oxide nanofibers will be demonstrated. Correlation between optical, structural, and electronic properties will be discussed.

Raman Spectroscopy

Fundamentals of Raman Spectroscopy

When monochromatic light is scattered from a molecule or crystal, most photons are elastically scattered, and the process is called Rayleigh scattering. It means that the energy ($h\nu_0$) and frequency (ν_0) of scattered photon have the same value as the

incident photon ($h\nu = h\nu_0$). However, only a small fraction of the light can be scattered at optical frequencies different from the frequency of the incident photons, which is usually lower than the frequency of inelastic scattering [1]. The process of inelastic scattering is called the Raman effect or Raman scattering. Raman scattering happens with a change in rotational, vibrational, or electronic energy of a crystal. If the energy (energy=Plank's constant*frequency) of the scattered photon is higher than the energy (frequency) of the incident photon, the Raman scattering is called anti-Stokes ($h\nu > h\nu_0$). On the other hand, when the frequency of scattered photon is lower than the frequency of the incident photon, it is called Stokes Raman scattering ($h\nu < h\nu_0$).

Figure 1 shows the basic processes which occur during Raman scattering. At room temperature, most molecules are present in the lowest vibrational level. The Raman scattering process from the ground vibrational level leads to absorption of energy by the molecule or crystal to the virtual energy level (1) and its "coming back" to the same vibrational level (2). This is called Stokes scattering. During anti-Stokes scattering (Figs. 1, 3, and 4), energy is transferred from excited atoms to the initial photon, and then the energy of an atom drops to a lower state. Because anti-Stokes scattering requires that the atoms were in a higher energy state, it takes place less frequently than the Stokes one.

The Raman shift is usually expressed in wavenumbers $\bar{\nu}$ (cm^{-1}), and it is expressed by the formula

$$\bar{\nu} = \frac{1}{\lambda_{inc}} - \frac{1}{\lambda_{scat}}, \tag{1}$$

where λ are the wavelengths (in cm) of the incident (λ_{inc}) and Raman scattered photons (λ_{scat}), respectively. In fact, Raman scattering is expressed as a shift in energy should be indicated as Δcm^{-1}, but it is often presented as cm^{-1}. In this case, Raman spectra consist of Raman intensity plotted vs. Raman shift (Fig. 2). Every Raman peak corresponds to a Raman shift from the incident light energy $h\nu_0$.

Raman spectroscopy is useful for chemical analysis and structural analysis [3]. There are many advantages of this method:

– **Specificity.** Raman peaks have a good signal-to-noise ratio, because it reflects some specific molecular vibrations. As a consequence, Raman spectra can be used as "fingerprints" of materials.

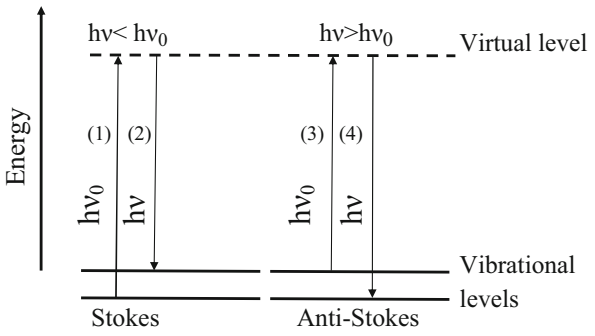

Fig. 1 Energy level diagram for Raman scattering

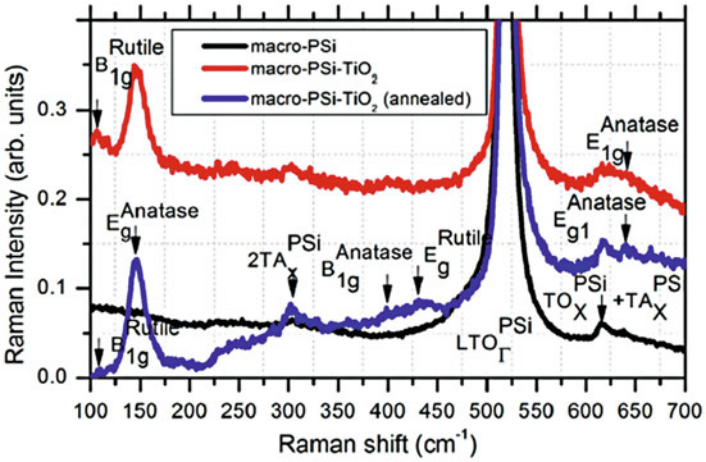

Fig. 2 Raman spectra of the macroporous silicon (macro-PSi) and TiO_2 films deposited onto macro-PSi before and after annealing [2]

- **Nondestructive:** Raman spectroscopy is a *nondestructive* technique, because it involves only the illumination of a sample.
- **Quantitative Raman:** Raman spectroscopy can be used for quantitative analysis. It allows to measure a relative concentration of molecules, because the intensity of Raman peaks is proportional to the number of molecules.
- **Short measurement times:** Raman spectroscopy allows to monitor chemical reactions in "real time," because acquisition time requires from seconds to several minutes.

Raman Techniques and Experimental Setups

The simple scheme of Raman spectrometer is shown in Fig. 3. The main components of the Raman spectrometer are a light source, excitation and delivery optic system, detector, and sample. The light source of a Raman spectrometer must give very intense radiation of monochromatic light. That is why in modern spectrometers, a laser radiation is used as a light source. Moreover, laser gives a polarized light, and this can be used to determine the depolarization ration [1]. The excitation wavelength is a crucial parameter for Raman spectroscopy. The choice of laser wavelength usually involves three factors: Raman cross section, detector sensitivity, and background scattering from the sample. Most Raman cross sections, which determine the probability of Raman scattering, decrease with increasing laser wavelength. In some cases when we need to improve sensitivity, shorter wavelengths should be used for detection which gives higher quantum efficiency and less noise. However, excitation by shorter wavelengths leads to a fluorescence which is a drawback for Raman spectroscopy measurements. Moving to higher wavelengths of excitation can significantly reduce fluorescence [4].

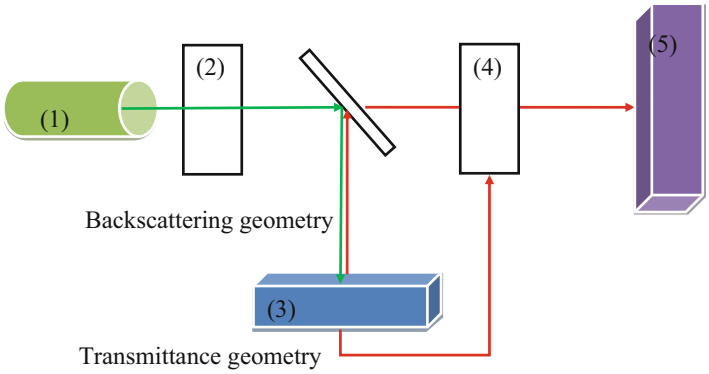

Fig. 3 The scheme of Raman spectrometer. (1) A laser excitation source, (2) excitation delivery optics, (3) a sample, (4) collection optics, (5) a detector and associated electronics

Many organic, and inorganic, materials are suitable for Raman spectroscopic analysis [5]. These can be solids, liquids, polymers, etc. Many powders and liquids can be examined by placing the container in which they are supplied directly in the beam. There are two basic geometries used in collecting Raman scattering: backscattering or 180° (b) and transmittance or 90° (t). In (t) scattering, the laser beam is passed through the sample, and the scattered light collected by the optical system at 90° goes to the detector. In the case of (b) scattering, the optical system collects the scattered light directly from the sample surface. It is very important to optimize each instrumental component for better efficiency because the Raman effect is relatively weak.

To collect Raman scattering effectively, it is necessary to remove the much more intense Rayleigh scattering. This can be done with two or even three monochromators. On the other hand, it is possible to use effective notch and edge filters which are widely used in modern Raman spectrometers. Notch filters are designed to absorb all light of the incident laser wavelength. The notch filter allows one to reduce the size of Raman spectrometers and enhance their efficiency. In most Raman spectrometers, notch filters are used to collect the scattered light, focusing it into a monochromator and then onto a detector – CCD (charge-couple device).

Raman Spectroscopy of Metal Oxide Nanofibers

Raman Spectroscopy of Metal Oxide

Metal oxides (MOx) are compounds/crystals formed from metal and oxygen atoms. Thus, the analysis and interpretation of Raman spectra for MOx requires understanding of how atoms move/vibrate in crystal lattices. The analysis of atomic motion is described by a field called lattice dynamics. The unit cell of the crystalline form is defined, and the motion of each atom in the unit cell is determined by solving the potential energy function of the lattice, which is the sum of all pairwise potential energies between each

pair of atoms. An important concept in the description of the motion of atoms in crystals (phonons) is the symmetry of the lattice. Group theory enables one to classify a crystal lattice according to what geometrical operations in space leave the lattice unchanged.

MOx occur in crystals in which the O^{-2} anions are often in close-packed sites, and the metal cations fit into tetrahedral or octahedral sites, with two tetrahedral sites per O^{-2} ion and one octahedral site per O^{-2}. To a large extent, this follows from the fact that the ionic radii of anions are significantly larger than that of the cations. In fact, relatively simple geometric arguments based on ionic radii enable predicting whether a particular anion will occupy tetrahedral or octahedral sites. Of course, the stoichiometry of the oxide will determine how many metal cations will be present, and details regarding the electronic states will play a role in determining the overall symmetry of the lattice [6]. As an example, we will consider ZnO monocrystal.

In ambient conditions, the thermodynamically stable phase of ZnO is the hexagonal wurtzite structure. The wurtzite structure belongs to the space group P63mc where the unit cell has four atoms (two metals and two oxygen). Each atom is tetrahedrally coordinated, i.e., the four next neighbors are of the other atom sort and located at the edges of a tetrahedron. The lattice has a hexagonal symmetry and is characterized by the lattice parameters a and c.

Four basis atoms determine the phonons dispersion in the wurtzite crystal. The possible displacements of atoms in the crystal unit cell are shown in Fig. 4. There are different phonon modes which are classified by direction of displacements. For instance, A and B modes are displacements along the c-axis. In this case, the A mode consists of a polarized oscillation of the rigid sublattices (Zn vs. O). On the other hand, the B modes are nonpolarized oscillations in opposite directions. Thus, A – polar mode – and B give two nonpolar modes. As atoms displace perpendicular to the c-axis, these modes are called E modes. Because the two axes are perpendicular to the c-axis, the E modes degenerate in twofold. As in the case of A and B modes, there is also one polarized mode, the E_1 mode (oscillation of rigid sublattices), and two nonpolarized modes, the E_2 modes, E_2(low) and E_2(high), which are associated

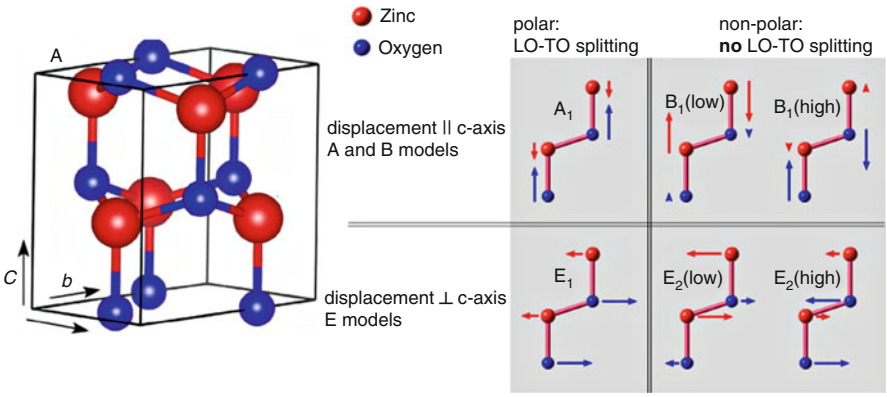

Fig. 4 The unit cell and optical phonon modes of ZnO wurtzite

with the vibration of the heavy Zn and light O sublattices, respectively. The E_2 modes are to be considered a Raman fingerprint for ZnO (Fig. 5).

Phonon Confinement Model (PCM)

Semiconductor crystals with sizes of a few nanometers typically contain several hundreds to several thousands of atoms; they are too small to have bulk electronic properties. Quantum confinement in such crystals arises due to the finite size of the crystal, which limits the motion of electrons, holes, and excitons. As a consequence, Raman spectroscopy can be a standard technique to study the nanostructured materials [8, 9]. Raman spectroscopy provides us information about phase, structure, and energy dispersion of nanocrystals. Mostly, the analysis of Raman spectra for nanostructures is based on the phonon confinement model (PCM) where the shape and crystallite size is taken into account [10, 11]. The finite size of nanocrystals leads to modifications of the vibrational properties.

A number of investigations have been performed to characterize the effects of finite size and 1D geometry (e.g., nanofiber) on the confinement of phonons. It was shown that the reduction of nanofiber diameter leads to downshifting and asymmetric broadening of the Raman line shape, which can be explained by the confinement of optical phonons. In bulk single crystals, the first-order Raman scattering is restricted by the momentum selection rules where phonon momentum is equal to zero ($q = 0$). However, the reduction of crystal size to nanometer values leads to the relaxation of this selection rule. Richter et al. have developed a model which described the phonon

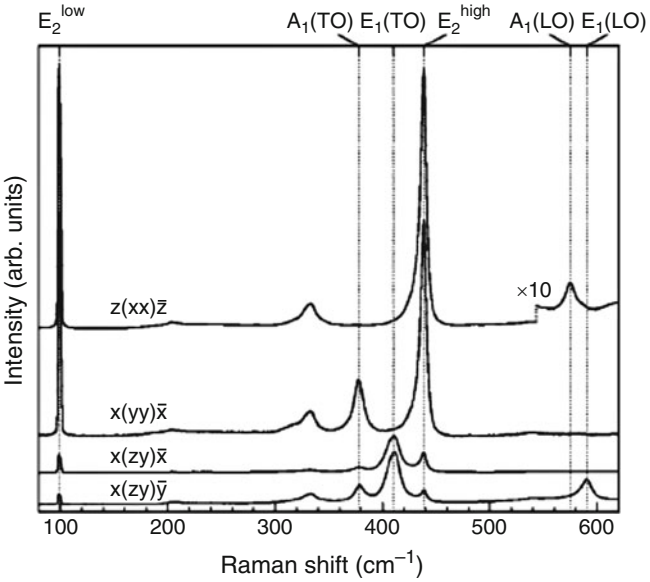

Fig. 5 Room temperature first-order Raman spectra of ZnO in scattering geometries corresponding to A_1+E_2 and E_1 symmetries [7]

dispersion in nanocrystals, including nanofibers [12]. In this model, the Gaussian-correlation functions have been used to describe the phonon dispersion.

The quantitative model that calculates the phonon spectrum of silicon nanocrystals has been developed by Campbell and Fauchet [13]. They also showed that this methodology could be spread to other semiconductors. The Raman spectrum is given by

$$I(\omega) \cong \int_{BZ} \frac{d^3q \ |C(0,q)|^2}{(\omega - \omega(q))^2 - \left(\frac{\Gamma_0}{2}\right)^2}; \tag{2}$$

where $|C(0,q)|^2 = \exp\left(-\frac{q^2L^2}{16\pi^2}\right)$, Γ_0 is the natural line width, $\omega(q)$ is the dispersion relation for optical phonons, and ω and q are the frequency and wavevector, respectively. We have used this methodology to estimate the average size of TiO_2 nanocrystallites in the PSi matrix [11, 14]. A simple confinement model has been used to calculate the shape of the 144 cm^{-1} mode of the anatase (the phase of TiO_2) at various nanocrystals sizes and to determine the average size of nanocrystallites.

Metal Oxide Nanofibers Examples

Mostly, in order to fabricate metal oxide nanofibers, one needs to produce a core polymer and then use different techniques to deposit metal oxides onto this core [15]. As a result, a core-shell structure will be obtained. Afterward, the polymer core could be removed or retained depending on the further application. Let us consider a few examples of MOx nanofibers and usage of Raman spectroscopy in their characterization.

Maensiri et al. have considered the sodium cobalt oxide ($NaCo_2O_4$) nanofibers with a diameter of 20–200 nm prepared by electrospinning [16]. The results of Raman spectroscopy (Fig. 6) allowed them to determine the phase and the composition of fabricated nanofibers before and after calcinations. Three main Raman

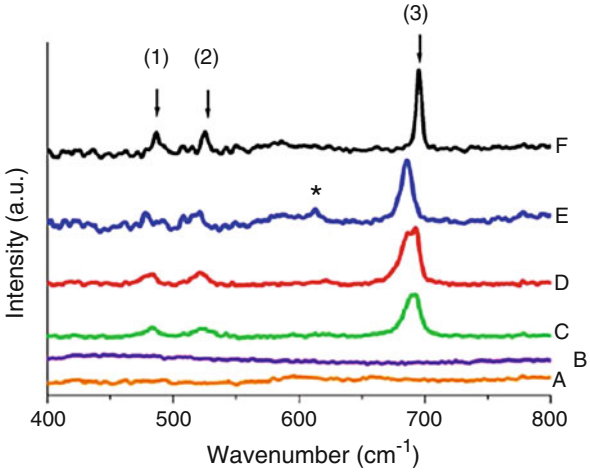

Fig. 6 Raman spectra of (**a**) studied fibers, (**b**) $NaCo_2O_4$ fibers, (**c**) $NaCo_2O_4$ fibers annealed at 300 C, (**d**) annealed at 400 C, (**e**) annealed at 800 C, (**f**) $NaCo_2O_4$ layers synthesized by solid-state reaction [16]

peaks at 480 cm^{-1} (E_{2g}), 521 cm^{-1} (E_{2g}), and 689 cm^{-1} (A_{1g}) were assigned to the space group of *P*63/*mmc*. For the nanofibers annealed at 800 °C, one can observe four Raman peaks at 480, 521, 613, and 689 cm^{-1}. The new peak at 613 cm^{-1} was assigned as E_{2g}. It was shown that the Raman-active mode in the $NaCo_2O_4$ corresponds to a frequency of 685–695 cm^{-1} (stretching modes of the Co–O). It is well known that this mode is very sensitive to any disorder. This allows us to study the nanofiber microstructure just by analyzing the shape of the Raman spectrum, its asymmetry, and the broadening. The peak asymmetry and broadening are attributed to the reduction of the photon lifetime and by the grain size, respectively. The broader the Raman mode, the smaller the grain size [16]. Besides, it is possible to estimate the grain size by using PCM.

Another example reports on structural characterization and morphology of TiO_2 nanofibers with diameters of 80–100 nm prepared by electrospinning and then annealed at above 300 °C in air for 3 h [17]. The anatase-to-rutile phase transition from TiO_2 nanofibers was studied by Raman spectroscopy. It is well known that anatase has six Raman-active modes: A_{1g}, $2B_{1g}$, $3E_g$, A_{2u}, and $2E_u$. In prepared TiO_2 nanofibers, authors observed six allowed Raman peaks at 144 cm^{-1} (E_g), 197 cm^{-1} (E_g), 399 cm^{-1} (B_{1g}), 513 cm^{-1} (A_{1g}), 519 cm^{-1} (B_{1g}), and 639 cm^{-1} (E_g). On the other hand, rutile has four active modes: 612 cm^{-1} (A_{1g}), 143 cm^{-1} (B_{1g}), 826 cm^{-1} (B_{2g}), and 447 cm^{-1} (E_g).

Nuansing et al. observed the main Raman peaks of anatase at 400 cm^{-1} (B_{1g}), 516 cm^{-1} (A_{1g} or B_{1g}), and 639 cm^{-1} (E_g) and of rutile at 449 cm^{-1} (E_g) and at 612 cm^{-1} (A_{1g}). These spectra were close to those in the bulk materials, except for their broader linewidth. Increasing the annealing temperature up to 800 °C, Raman peak linewidths become smaller, and their intensities increase. The temperature of anatase-to-rutile phase transition has been estimated by comparing the ratio of Raman peaks intensity. As it was shown, the anatase phase was distinct in TiO_2 nanofibers annealed at 400–600 °C. After annealing at 700–800 °C, the peaks corresponding to rutile phase (449 cm^{-1} (E_g), 612 cm^{-1} (A_{1g})) begin to intensify relative to the anatase peaks. Nuansing et al. showed a significant effect of annealing temperature on the crystalline phase and the morphology of the TiO_2 nanofibers (Fig. 7).

Fourier Transform Infrared (FTIR) Spectroscopy

Fundamentals of FTIR Spectroscopy

Infrared (IR) spectroscopy and Raman spectroscopy are techniques dealing with molecular vibrations. IR spectroscopy analyzes vibrations, which modulate the molecular dipole moment, while Raman spectroscopy studies vibrations, which modulate the polarizability. It is therefore appropriate to evaluate infrared and Raman spectra jointly.

IR spectroscopy is a technique based on a measurement of absorbed infrared radiation passing/reflecting through a sample. Every IR peak corresponds to molecular vibration frequency. IR spectroscopy recording with interferometers, followed

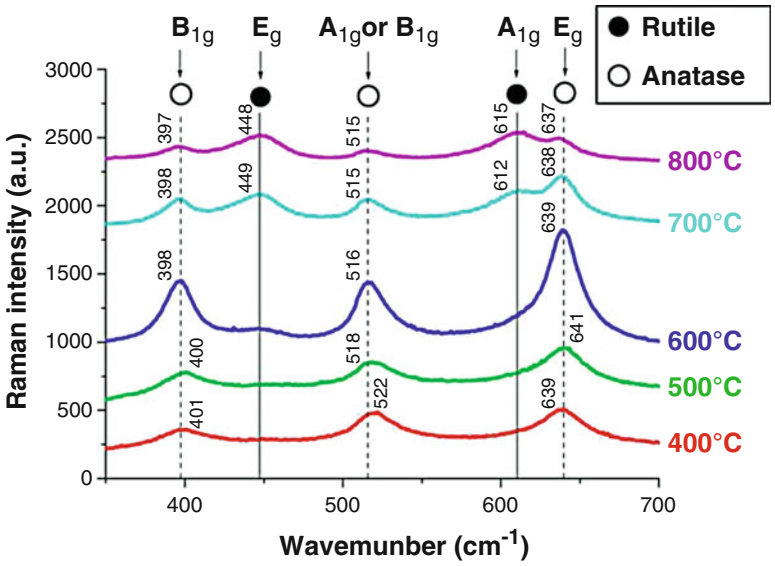

Fig. 7 Raman spectra of electrospun TiO_2/PVP composite nanofibers calcined in air for 3 h at different temperatures [17]

by the Fourier transformation of the interferogram into a spectrum, is called FTIR spectroscopy. FTIR spectroscopy was developed in order to overcome the limitations encountered with dispersive instruments [18].

The infrared spectrum (10–14,000 cm^{-1}) can be split into three main regions: near-IR, mid-IR, and far-IR. The most commonly used region for analysis is the mid-IR (400–4000 cm^{-1}). Mid-IR spectroscopy is based on investigation of the interaction between molecules and incident IR radiation. As was previously mentioned, passing through the sample, specific wavelengths of IR radiation are absorbed which leads to the chemical bonds in the material to undergo different types of vibrations (stretching, bending, and contracting). Different molecular functional groups tend to absorb IR radiation in the same frequency/wavenumber range regardless of molecular structures. This gives an opportunity to determine the chemical structures in the molecule. Mostly, IR spectra are measured by calculating the intensity of transmittance/absorbance IR radiation (Y-axis) vs. wavenumber units (X-axis) [19].

FTIR spectroscopy does not give us a detailed information about a molecular formula or its structure. However, it provides useful data about the molecular fragments and molecular functional groups. Therefore, other techniques and methods should be performed with FTIR in order to provide complete information about the molecular structure.

It is worth to emphasize some advantages of FTIR spectroscopy [20]:

- Relatively **fast and simple** to use: Little or no sample preparation required for spectral acquisition.
- **Sensitive** method that requires a very little sample.

- **Nondestructive.**
- **Qualitative** as well as **quantitative analysis.**
- **Multiple sample environment**: Samples in the form of liquid, gas, powder, solid, or film can be tested.

FTIR Spectrometers and Measuring Principals

In the conventional FTIR spectrometer, in order to disperse light into individual frequencies, a grating or a prism is used [21]. However FTIR spectrometers work on a different principle – *Fourier transform (FT). Interferograms (explained later)* which arise from the interference of radiation between two beams are used in FTIR spectroscopy.

The main components of FTIR spectrometers are shown in Fig. 8. Mostly a Michelson interferometer is used in FTIR spectrometry, which consists of two perpendicular mirrors separated by a semi-reflecting film, the *beam splitter*, and one of the mirrors can travel in a direction perpendicular to the plane. The superposition of these two beams reflected from mirrors and, returning back, recombined and interfered. The moving mirror produces an optical path difference $((n + 1/2)\lambda)$ between two beams causing the destructive or constructive interference. Because the optical path of the "traveling" beam has a fixed length and the path of the second beam is constantly changing due to mirror movement, the interfering signal is the result of these two beams and is called an interferogram. The interferogram has a unique property: it measures all frequencies simultaneously, and as a consequence, it does not require a lot of time. However, interferogram cannot be interpreted directly. Thus, it should be "decoded" by using a well-known mathematical method – the Fourier transformation (FT). An FTIR spectrometer collects and digitizes the interferogram, performs the FT function, and displays the spectrum.

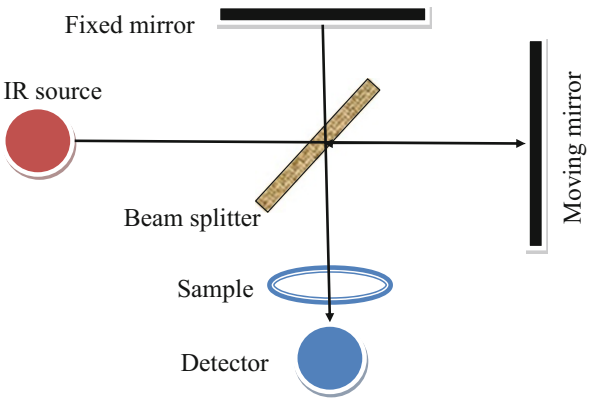

Fig. 8 Schematic diagram of a FTIR spectrometer based on Michelson interferometer

The mathematical expression of FT can be expressed as

$$F(\omega) = \int_{-\infty}^{\infty} f(x) e^{i\omega x} \mathrm{dx}. \tag{3}$$

And the reverse Fourier transform is

$$f(x) = \frac{1}{2\pi} \int_{-\infty}^{\infty} F(\omega) e^{-i\omega x} d\omega, \tag{4}$$

where x is the optical path difference and ω is angular frequency. $f(x)$ is the interferogram, which is determined experimentally, and $F(\omega)$ is the IR spectrum.

FTIR Spectroscopy of Metal Oxide Nanofibers

As was mentioned previously, FTIR spectroscopy allows us to detect functional molecular groups on the surface of studied materials. Using the FTIR spectroscopy, desorption and adsorption process on the surface of nanofibers can be also trailed.

Imran et al. have shown that by using the FTIR spectroscopy, it is possible to track the effect of calcination on the morphology and phase structure of ZnO nanofibers fabricated by electrospinning [22]. Figure 9 shows the FTIR spectra of

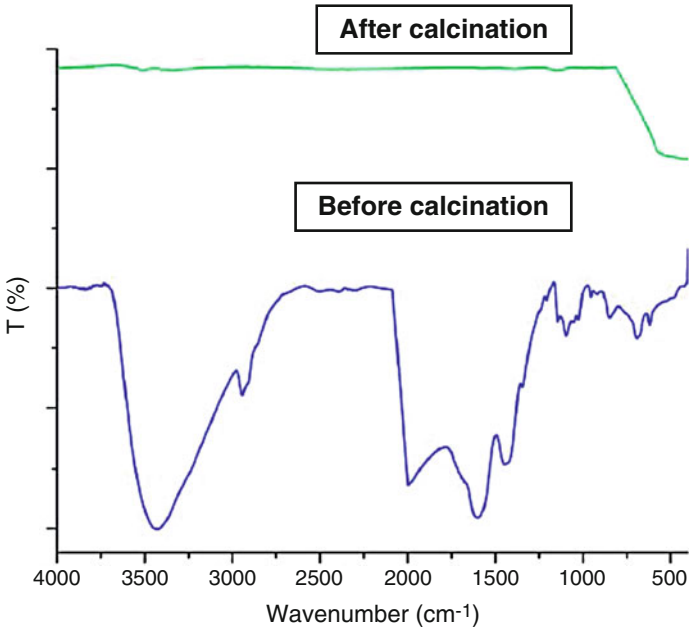

Fig. 9 FTIR spectra of 15% zinc acetate/PVA precursor nanofibers (before calcination) and ZnO nanofibers (after calcination) [22]

zinc acetate/PVA (polyvinyl alcohol) precursor and calcined nanofibers at 480 °C for 6 h. Before calcination, the strong cyclic bands between 500 and 2000 cm^{-1} may be attributed to the stretching and bending frequencies of O-H, C=C, and C-H of PVA. After calcination, it is clearly seen that all PVA peaks are vanished and only one well-defined peak of ZnO at 472 cm^{-1} is presented in the spectrum, confirming the presence of ZnO and the decomposition of the PVA.

The presence of Cu-O bands in CuO electrospun nanofiber was also confirmed by FTIR spectroscopy by Sharma et al. [23].They have shown that the large band between 4000 cm^{-1} and 3500 cm^{-1} corresponds to the O-H stretching. Other bands observed between 2800 cm^{-1} and 1680 cm^{-1} refer to the stretching C-H from the alkyl groups and are due to the stretching C=O and C-O from acetate groups remaining from PVA. However, a peak around 570 cm^{-1} was assigned to Cu-O of copper oxide, indicating that the fiber had pure inorganic CuO species.

To confirm the composition of cobalt oxide/iron oxide composite nanofibers, Asif et al. have used FTIR spectroscopy [24]. The M-O-M stretching mode at 640 cm^{-1} was observed on FTIR. This data allowed them to confirm that the composite nanofibers are metal oxide-based nanostructures.

FTIR spectroscopy of MOx nanofibers gives also a possibility to detect the interaction between various functional groups in the composite. For instance, Patil et al. have studied the PANI (polyaniline) and PANI/ZnO nanofibers by FTIR spectroscopy [25]. Authors have shown that the peaks in the range 3380 cm^{-1} correspond to N-H band stretching vibration. Comparing these peaks of pure PANI, the peaks of PANI/ZnO, they found the shift of peaks toward lower wavenumbers. They explained this shifting by the interaction of hydrogen bonding between the hydroxyl and the amine groups on the surfaces of ZnO and PANI molecular chains, respectively.

UV-Visible Optical Spectroscopy for Investigation of Metal Oxide Nanofibers

Main Fundamental Optical Parameters of Metal Oxide Nanostructures

Band gap of metal oxide is one of the important optical parameters. In general, band gap is a minimal energy of an absorbed photon to generate free electron-hole couple in conductance and valence bands of metal oxide (Fig. 10).

Due to structure defects and dangling surface bonds, electronic states can appear nearby conductance and valence bands. They have nonlinear distribution in the band gap. As a result, optical transitions between these states with energy E_g^* take place. As it can be seen from Fig. 2, $E_g > E_g^*$, and these states are called "Urbach tail." From Fig. 11, the Urbach tail value can be calculated from the figure as

$$E_u = E_g - E_g^*. \tag{5}$$

The Urbach tail can point to a number of defects and their distribution into the band gap [26].

Photoluminescence is an effect of light emission due to the interaction of absorbed light with metal oxide. Photoluminescence process in metal oxides is generalized in Fig. 12. The photoinduced electrons and holes can be captured on defect sites and then recombine with light emission. The energy of emitted light will always be lower than the energy of absorbed light (transitions ***a–d***, Fig. 12). In addition, electrons and holes can recombine without light emission (transitions ***e***, Fig. 12).

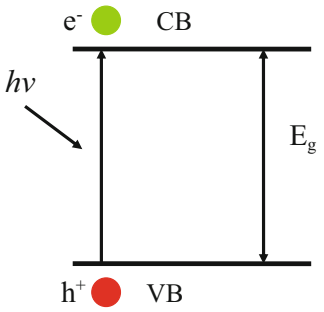

Fig. 10 Optical transition of electron between valence and conductance bands of metal oxide, induced by photon absorption

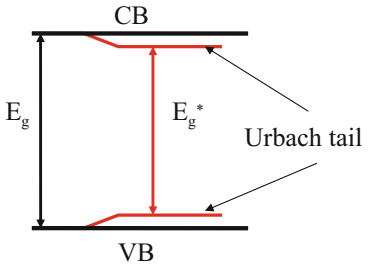

Fig. 11 Formation of Urbach tail in a band gap of metal oxide

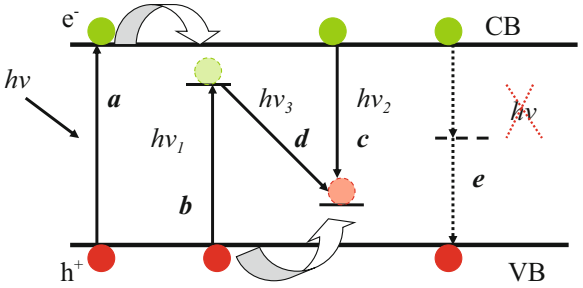

Fig. 12 Scheme of photoluminescence in metal oxide with optically active sites in the band gap: *a* light absorption and generation of free electrons and holes; *b* recombination of free hole with electron, bound on a defect site with emission of photon $hv_1<hv$; *c* recombination electron of free hole with emission of photon $hv_2<hv$, bound on a defect site; *d* donor-acceptor recombination with emission of photon $hv_3<hv$; *e* nonradiative recombination of electrons and holes

Photoluminescence spectroscopy can provide information about structure defects, their types, and activation energies. Photoluminescence properties of metal oxide point to possible applications of metal oxide nanofibers in photocatalysis, optical sensing, etc. [27].

Restriction of Traditional Methodologies for Optical Characterization of Metal Oxides

Traditional optical spectroscopy (transmittance/absorbance) is based on the Beer-Lambert law:

$$I = I_0 \cdot e^{-\alpha \cdot d}, \tag{6}$$

where I, I_0, α, and d are intensity of transmitted/reflected light, intensity of the incident light, absorption coefficient, and thickness of the samples (applicable for thin films). It is expected that the investigated sample is homogeneous and deposited on transparent substrate. In this case, transmittance measurements provide information about absorbance spectrum of the samples.

When the sample is deposited on opaque (nontransparent) substrate, reflectance spectroscopy is needed. The Beer-Lambert law will involve the parameter I as the reflected signal. Reflectance spectroscopy has been much improved in ellipsometry through measurement of reflectance spectra at different incidence angles of light. Ellipsometry can provide extinction coefficient and refractive index of the investigated samples [26].

However, transmittance, reflectance, and ellipsometry are applicable only to thin films, deposited on flat substrates. Complex calculations are needed for samples with several phases or components. These methodologies are not applicable for investigation of optical properties of 1D nanostructures due to nonhomogeneity of 1D nanostructure layer/scaffold and strong light scattering effect [26].

Diffuse Reflectance Spectroscopy for Characterization of Metal Oxide Nanofibers

Basis of the Diffuse Reflectance Spectroscopy

Diffuse reflectance is the only one correct method to analyze absorbance spectra of 1D metal oxide nanostructures. An integrating sphere is used to measure diffuse reflectance (Fig. 13). The sphere is constructed to collect reflections coming from 1D nanostructures in a wide range of reflected angles.

The diffuse reflectance spectrum will be dependent on the measured reflectance $\boldsymbol{R}$ vs. wavelength $\boldsymbol{\lambda}$. In order to calculate absorption, the Kubelka-Munk equation should be used [27]:

$$F = \frac{(1-R)^2}{2 \cdot R}, \tag{7}$$

where $\boldsymbol{F}$ and $\boldsymbol{R}$ are absorbance and reflectance ($\boldsymbol{R}$ value should be divided by 100%) for wavelength $\boldsymbol{\lambda}$.

Application of Diffuse Reflectance Spectroscopy for Analysis of Optical Properties of 1D Nanofibers

The experimental dependence $F(\lambda)$ provides information about absorption edge of metal oxide nanofibers and their band gap. However, one important issue should be noticed before calculations. It is known that semiconductors in general are divided into two main groups with direct optical and indirect optical transitions [27, 28]. In terms of energy $\boldsymbol{E}$ and wavevector $\boldsymbol{k}$, the direct optical transitions occur without phonon generation ($\boldsymbol{k} = 0$) (Fig. 14a) and indirect optical transition occur with phonon generation ($\boldsymbol{k} \neq 0$) (Fig. 14a). Absorption coefficient $\boldsymbol{F}$ and band gap of 1D metal oxide nanostructures $\boldsymbol{E_g}$ will be related to the following equation:

$$\text{For direct optical transitions } (F \cdot \text{hv})^2 \sim \left(\text{hv} - E_g\right) \tag{8}$$

$$\text{For indirect optical transitions } (F \cdot \text{hv})^{\frac{1}{2}} \sim \left(\text{hv} - E_g\right) \tag{9}$$

Equations 4 and 5 will be used for evaluation of band gap value of 1D metal oxide nanostructures. The most well-known metal oxide nanofibers with direct optical transitions are ZnO and SnO_2, whereas TiO_2 nanofibers have indirect optical transitions. More information of the band gaps and optical properties of generally used metal oxide nanofibers is presented in Table 1.

More practical examples of diffuse reflectance application for analysis of metal oxide nanofibers are given below. Lavanya et al. reported on reduced graphene oxide

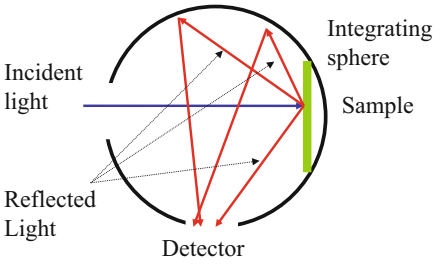

Fig. 13 Scheme of diffuse reflectance measurements with integrating sphere

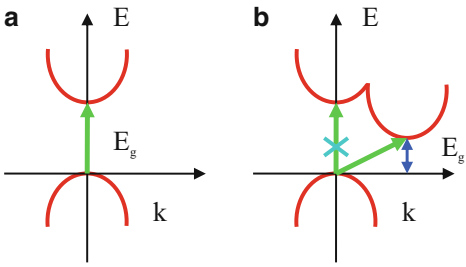

Fig. 14 Dispersion diagram with direct (**a**) and indirect optical transitions (**b**)

(rGO) wrapped anatase/rutile mixed phase TiO_2 nanofibers for photocatalytic applications [37]. TiO_2 nanofibers were deposited by electrospinning from titanium tetraisopropoxide mixed with polyvinylpyrrolidone (PVP) solution. After deposition the TiO_2 nanofibers were annealed at 600 °C.

The rGO was mixed with TiO_2 nanofibers in ratios of 1:0.25, 1:0.5, and 1:1. The obtained samples were referred as MPTNFG-1, MPTNFG-2, and MPTNFG-3, respectively. Diffuse reflectance spectra were converted to absorbance spectra according to Eq. 3 (Fig. 14a). The band gap values were calculated as for indirect optical transitions (Eq. 5). As it is seen from Fig. 14b, the band gap value was estimated as the intersection of the linear part of the plot with horizontal axis [37]. The estimated band gaps are 3.26 eV, 3.17 eV, 3.06 eV, and 3 eV for MPTNFs, MPTNFG-1, MPTNFG-2, and MPTNFG-3, respectively. Thus, from diffuse reflectance measurements, one can conclude that the increase of rGO results in the decrease of the band gap of TiO_2 nanofibers (Fig. 15).

Diffuse reflectance spectroscopy can be effective to evaluate structure changes of metal oxide nanofibers during different treatments. Lepcha et al. (2015) used optical spectroscopy to investigate the influence of H_2 plasma treatment at different temperatures [39]. Band gap shift to lower values and additional absorption peaks that

Table 1 Band gaps and optical parameters of metal oxide nanofibers

Nanofibers	Type of band gap	Band gap value, eV	Source
ZnO	Direct	3.2–3.3 (non-doped)	[29–31]
		3.3–3.5 (Al doped)	
SnO_2	Direct	3.6–3.7	[32]
Fe_2O_3	Direct	2.2–2.3	[33]
In_2O_3	Direct	2.78–2.94	[34, 35]
Cu_2O	Direct	2.2	[36]
TiO_2	Indirect	3–3.2	[37]
CuO	Indirect	1.2–1.7	[38]

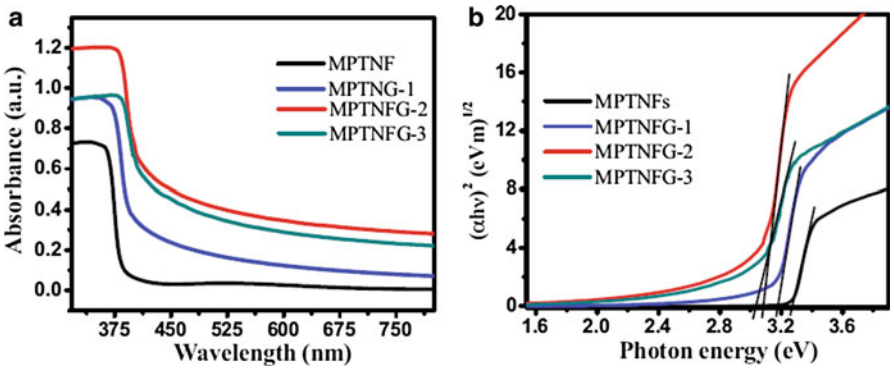

Fig. 15 Absorbance spectra (**a**) and band gap calculation (**b**) of TiO_2-rGO nanofibers [37]

were found after plasma treatment resulted from oxidation of Ti^{4+} ions to Ti^{3+}. Lu et al. (2017) investigated nitrogen doping of In_2O_3 nanofibers. Due to forming of InN phase, the band gap of N-In_2O_3 nanofibers significantly decreased with an increase in dopant concentration [35].

Diffuse reflectance spectroscopy is an effective method for analysis of optical properties of metal oxide composites. Chae et al. (2017) investigated forming of CeO_2-Cu_2O composite nanofibers [36]. Absorbance spectra of the CeO_2 nanofibers showed absorption in the range of 390–440 nm (Fig. 16a). The composite CeO_2-Cu_2O nanofibers showed an additional absorption band in the range 570–610 nm, related to Cu_2O (Fig. 16b). Red shift of absorption edge was observed after forming CeO_2-Cu_2O composites [36].

Hao et al. (2015) showed fabrication of TiO_2 nanofibers, decorated with Au nanoparticles for photocatalytic applications [40]. Optical properties were studied with diffuse reflectance spectroscopy. It was shown that band gap of TiO_2 decreased with an increase in Au concentration. New absorption peak in the region of 450–580 nm was found after forming TiO_2/Au composites. The peak corresponded to surface Plasmon resonance in Au nanoparticles. The width and position of the peak changed depending on the concentration of Au nanoparticles on TiO_2 surface [40].

Doping of metal oxides can result in the enhancement of charge carriers. At high doping concentration, the Fermi level moves to CB for n-type metal oxides, and it moves to VB for p-type metal oxides. Metal oxide becomes a degenerative semiconductor. The increase of the charge concentration makes a significant impact to optical properties of metal oxide nanofibers. This doping effect is known as the

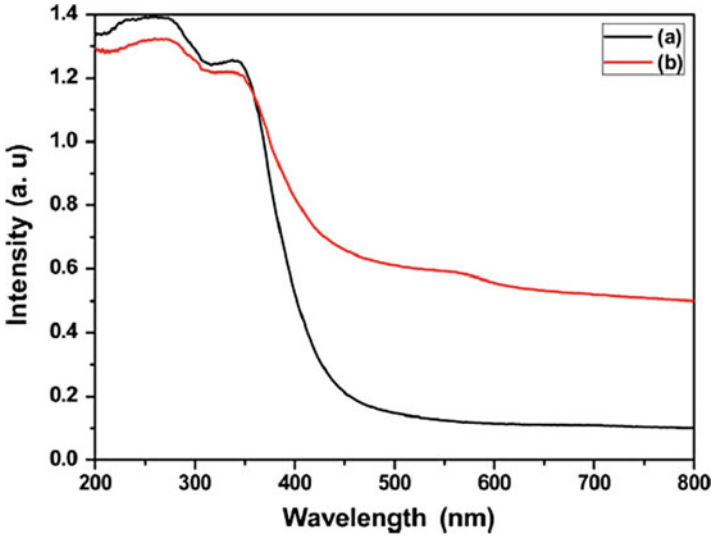

Fig. 16 Absorbance spectra of CeO_2 (**a**) and CeO_2-Cu_2O composite (**b**) nanofibers calcined at 500 °C [36]

Burstein-Moss effect. The Burstein-Moss effect is supported by a blue shift of band gap value of metal oxide nanofibers (Fig. 17).

Feng et al. (2011) calculated band gap values of Al-doped ZnO nanofibers. The band gap value increased from 3.28 to 3.38 eV with an increase in Al-doping concentration from 0% to 3 atm. % [29]. Similar results were observed for other Al-doped ZnO nanofibers reported by Chen et al. (2014) and Cho et al. (2016) [31, 41].

Kuo et al. have performed a calculation of electron concentrations in In_2O_3 nanofiber dopes with Sn [34]. According to Kuo et al., the band gap of metal oxide nanofibers $\boldsymbol{E_g}$ depends on the concentration of free electrons $\boldsymbol{n}$ as [34]

$$E_g = E_{g0} + \frac{h^2}{8 \cdot m^*} \cdot \left(\frac{3}{\pi}\right)^{2/3} \cdot n^{2/3} \tag{10}$$

where E_{g0}, h, and m^* are band gap of undoped In_2O_3 nanofibers, Plank's constant, and effective mass of electron, respectively. The calculated values of free electron concentrations were $5.96 \cdot 10^{18}$, $3.49 \cdot 10^{19}$, and $1.41 \cdot 10^{20}$ cm^{-3} for In/Sn ratios 9:1, 8:2, and 7:3, respectively. For comparison, the carrier concentration of undoped In_2O_3 was estimated as $3.7 \cdot 10^{17}$ cm^{-3}.

Urbach tail is one of important parameters to estimate optical defects presence and structure disorder (amorphous/crystalline) value. It can be calculated from absorption spectrum using following equation [27]:

$$F = F_0 \cdot e^{\frac{hv - E_0}{E_u}} \tag{11}$$

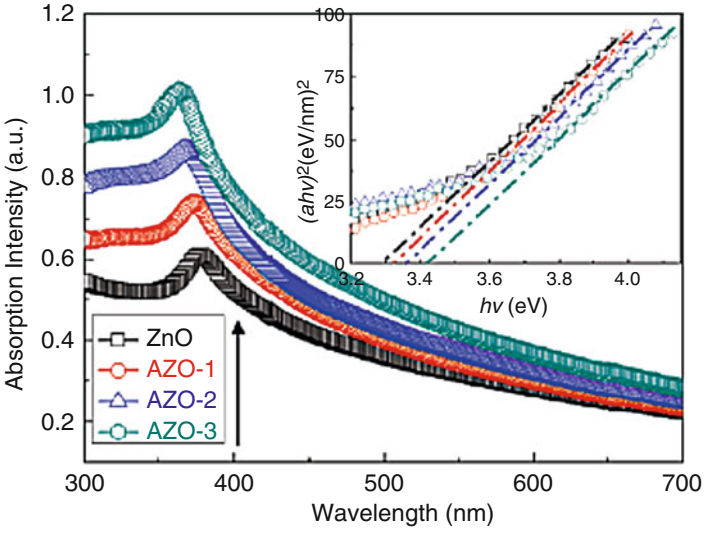

Fig. 17 Absorption spectra of Al-doped ZnO (AZO) nanofibers. Al concentration increases from sample AZO-1 to AZO-3 [29]

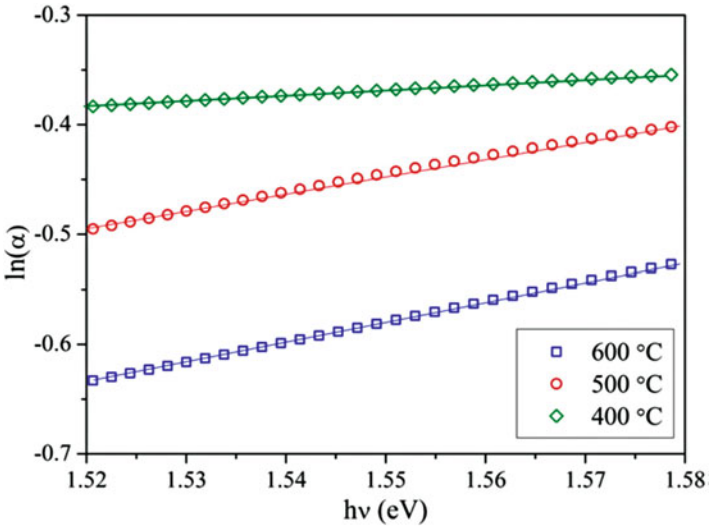

Fig. 18 Urbach tail calculation for Co_3O_4 nanofibers, calcined at different temperatures [42]

$\boldsymbol{F_0}$ and $\boldsymbol{E_0}$ are material parameters, **hv** and $\boldsymbol{E_u}$ are photon energy and Urbach energy, respectively. Parameter F was calculated using Eq. (11).

George et al. (2015) have investigated optical properties of Co_3O_4 nanofibers, calcined at different temperatures [42]. Urbach tail values were obtained from the plots of ln(α) vs. hv (Fig. 18). The obtained Urbach tail values were inversely proportional to the slope of the plots in Fig. 9. The obtained values of Urbach tail were 1.91, 0.65, and 0.55 eV for calcination temperatures 400, 500, and 600 °C, respectively [42]. The obtained results point to improvement of crystalline structure after thermal treatment.

Thus, diffuse reflectance spectroscopy provides information on band gap changes of metal oxide nanofibers during different treatments (doping, annealing, composite, etc.). Urbach tail values, calculated from absorbance spectra, provide information about local states in band gap of metal oxide and value of structure disorder. Numerical calculations of electron concentrations for Burstein-Moss effect can be combined with electrical measurements for modeling and tuning of fundamental properties of metal oxide nanofibers.

Photoluminescence Spectroscopy for Characterization of Metal Oxide Nanofibers

Steady-State Photoluminescence Spectroscopy for Characterization of Metal Oxide Nanofibers

Photoluminescence (PL) is a powerful method in analyzing light emission properties of 1D metal oxide nanostructures. Photoluminescence (PL) setup is demonstrated in Fig. 19.

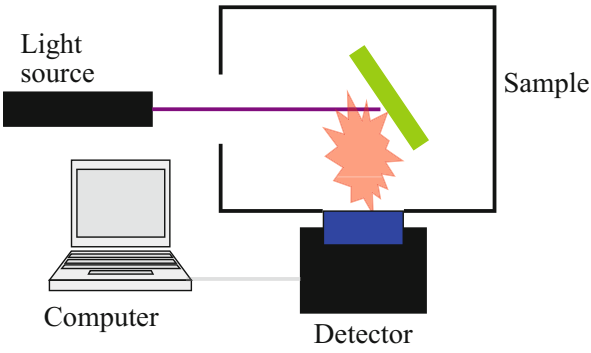

Fig. 19 Photoluminescence setup for characterization of 1D metal oxide nanofibers

The excitation light from light source-induced photoluminescence is collected by a detector and worked out by computer software. Lasers, light-emitting diodes (LED), and arc lamps are used as light sources [27, 43]. Photomultipliers with monochromators, CCD cameras, and optical fiber spectrometers are used as light detectors [27, 43]. As most of metal oxides are wide band gap materials, typical wavelengths for PL excitation vary from 266 to 405 nm, produced by a number of solid-state lasers and UV LEDs.

PL of the metal oxide nanofibers can be measured in a wide range of temperatures (2–300 K). Measurements at low temperature require special equipment. Therefore, in this section we will focus on measurements at room temperature as the rapid and simple method to analyze optical properties of metal oxide nanofibers.

Photoluminescence is a quite effective method for fast and nondestructive phase analysis in titania nanofibers [44]. It is known that TiO_2 exists in two main phases rutile and anatase [44]. Phase transitions between anatase and rutile appear under thermal treatment of TiO_2 nanofibers at the temperatures higher than 600 °C [44]. Zone diagrams and photoluminescence schemes of anatase and rutile phases TiO_2 nanofibers are shown in Fig. 11. Band gaps of anatase and rutile titania nanotubes are 3.2 and 3 eV, respectively [44]. Thus, the PL emission in anatase titania nanofibers will be in the visible ($\mathbf{hv_1}$) range and IR range ($\mathbf{hv_2}$). The PL emission in rutile titania nanofibers will be only in IR range ($\mathbf{hv_3}$). Moreover, it was shown that $\mathbf{hv_2} > \mathbf{hv_3}$ up to 0.4–0.6 eV [44]. Defect states act as photoluminescence centers in TiO_2 nanofibers. In anatase nanofibers oxygen vacancies (neutral and ionized) and self-trapped excitons form emission band in the range of 430–560 nm. Surface states of Ti^{3+} and other structure defects are responsible for emission in the range of 580–700 nm. In rutile nanofibers Ti^{3+} states form emission in the range of 790–810 nm [44].

In Fig. 20, one can see PL spectra of TiO_2 nanofibers, annealed at different temperatures. Anatase phase was formed at a lower temperature and anatase-to-rutile phase transition occurred at high temperature. The measured PL clearly showed a difference between anatase and rutile (Fig. 20). Deconvolution of the PL peaks using Gaussian function provides information about photon energies emitted from different defect levels [44].

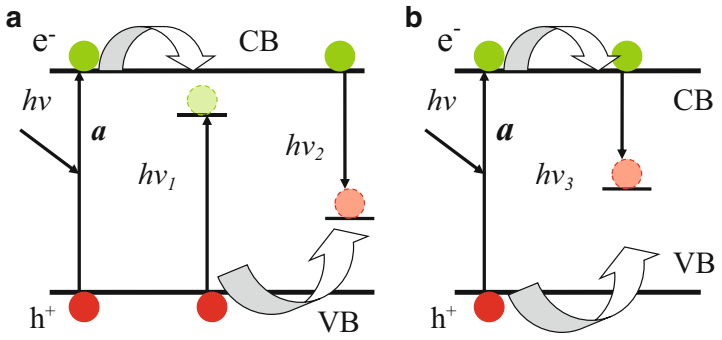

Fig. 20 Photoluminescence scheme in TiO_2 nanofibers: (**a**) anatase; (**b**) rutile

TiO_2-based composite materials have wide applications in catalysis and photocatalysis. Photoluminescence is one of the methods to control composite formation. Nasr et al. (2017) have investigated electrospun TiO_2 anatase nanofibers, doped with boron nitride [28]. The PL of non-doped TiO_2 nanofibers showed a wide peak in the range of 420–700 nm. The BN doping resulted in increase of photoluminescence intensity of TiO_2 nanofibers. The proposed explanation addressed to suppressing of nonradiative recombination through passivation of surface states by boron nitride.

Lavanya et al. investigated an effect of graphene oxide (GO) doping of TiO_2 nanofibers by photoluminescence spectroscopy [37]. It was shown that PL intensity of TiO_2 nanofibers significantly decreased due to charge separation at GO/TiO_2 interface. As charge separation is important for photocatalytic applications, the study of PL changes can reveal the effectiveness of charge separation.

Ahn et al. (2016) have reported on SnO_2/TiO_2 composite nanofibers. TiO_2 nanolayers were formed over SnO_2 nanofibers by chemical bath growth [45]. SnO_2 nanofibers demonstrated wide emission peak, centered at 550 nm. Deposition of TiO_2 shell over SnO_2 nanofibers led to complete quenching of SnO2 photoluminescence. Possible mechanism of PL quenching was a formation of the heterostructure between SnO_2 and TiO_2. The photogenerated electrons transferred from conductance band of SnO_2 to conductance band of TiO_2 reducing possibility of photoluminescence [45] (Fig. 21).

Zhang et al. (2014) reported on TiO_2, TiO_2/SnO_2, and Pt-TiO_2/SnO_2 composite nanofibers by electrospinning [46]. The bare TiO2 nanofibers showed a wide emission band in the range of 400–500 nm (Fig. 22a). Forming of TiO_2/SnO_2 nanocomposites resulted in quenching of PL intensity (Fig. 22b). Deposition of Pt nanostructures on the surface of TiO_2/SnO_2 nanofibers increased the quenching effect. The quenching mechanism is related to the transfer of photogenerated charge from TiO_2 to SnO_2 and Pt [46].

Zinc oxide-based nanofibers are one of the most widespread nanomaterials. Due to high band gap and unique properties, ZnO nanostructures demonstrate two emission bands: UV (near band edge) at 370–390 nm and VIS (deep level emission) at 440–720 nm [27, 47] (Fig. 23).

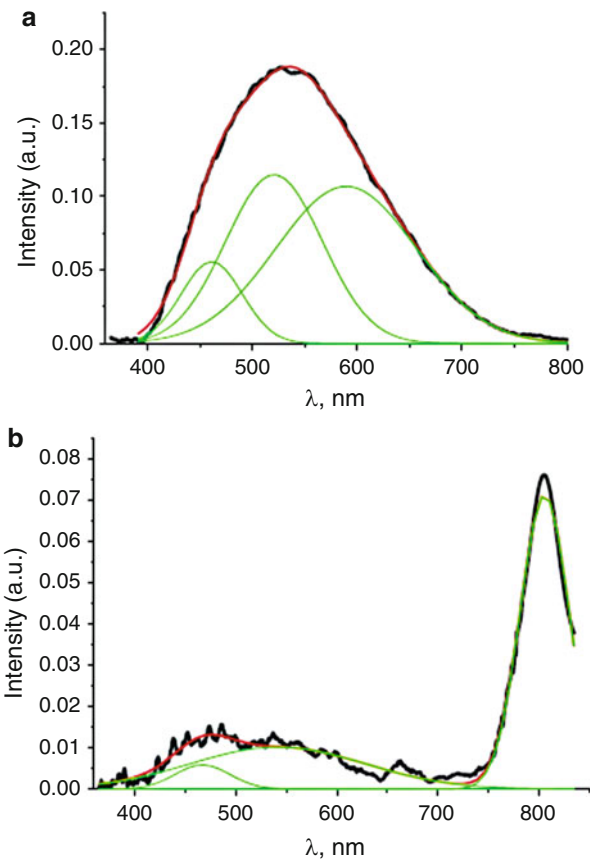

Fig. 21 Photoluminescence of TiO_2 nanofibers annealed at 500 °C (**a**) and 900 °C (**b**) [44]

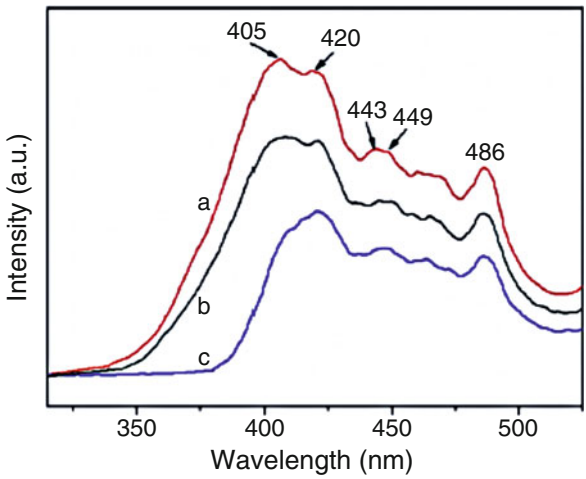

Fig. 22 Room-temperature PL spectra of (**a**) the bare TiO2 nanofibers, (**b**) TiO_2/SnO_2 nanofibers, and (**c**) the Pt-TiO_2/SnO_2 nanofibers [46]

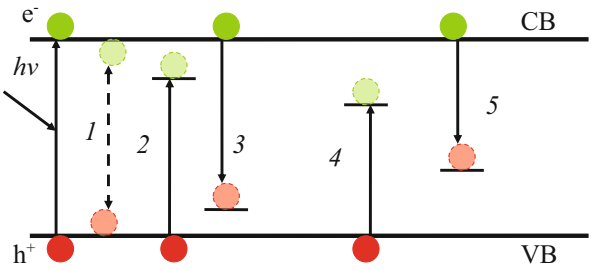

Fig. 23 Luminescence centers in ZnO nanorods: 1–3 near band edge emission, 4–5 deep level emission

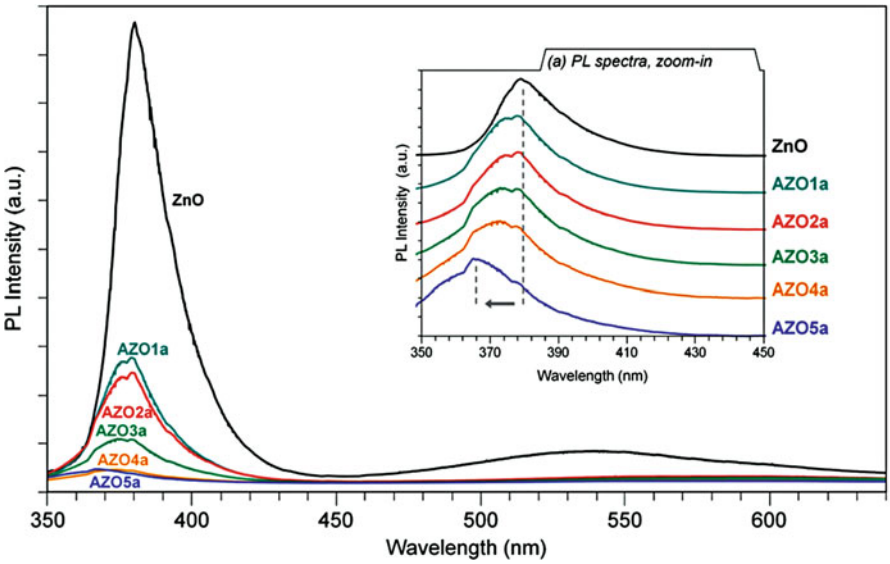

Fig. 24 Photoluminescence spectra of ZnO and five AZO nanofibers. Inset illustrates the rescaled spectra showing the blue-shifted UV emissions [31]

Optical transitions 1 (Fig. 24) correspond to quasiparticle called excitons. The exciton is an electron-hole couple, which can dissociate (electrons and holes transfer to CB and VB, respectively) or recombine with photon energy, close to the band gap of ZnO. The exciton dissociation energy, called exciton binding energy, is 0.06 eV, which is the highest value for semiconductors. Thus, excitons are present in ZnO even at room temperatures. Optical transitions 2–3 correspond to shallow states formed by structure defects. Optical transitions 4–5 correspond to defects, formed by Zn interstitials, O interstitials, Zn vacancies, and O vacancies [27, 47]. In addition, doping elements can form luminescence states in the band gap of ZnO. Despite ZnO being a well-studied material, no general model of the PL mechanisms in ZnO has been developed.

Cho et al. (2016) have analyzed Al-doping effect of ZnO nanofibers with photoluminescence (Fig. 24). The developed nanofibers were marked as ZnO,

AZO1a, AZO2a, AZO3a, AZO4a, and AZO5a, which correspond to Al/Zn atomic ratios of 0%, 1%, 2%, 3%, 4%, and 5%, respectively [31]. The samples were annealed at 600 °C. The photoluminescence spectra, presented in Fig. 24, showed a significant decrease of PL intensity. Blue shift of near band edge emission was found. This was explained by the increase of the band gap of the AZO nanofibers due to the Burstein-Moss effect [31]. It is known that in intense UV emission and high ratio of UV-VIS emission, high nanostructures point to high crystallinity of ZnO nanostructures. Therefore, doping of ZnO with Al atoms results in a decrease of crystallinity of ZnO nanofibers and leads to quenching of UV band of PL. The quenching of visible emission and the passivation of oxygen vacancies were explained by Al dopants [31]. Thus, the changes of PL spectra could point to the changes in crystalline structure of ZnO-based nanofibers.

Santangelo et al. reported on optical properties of pure and Al-, Ca-, and Al-Ca-doped electrospun ZnO nanofibers [48]. The nanofibers were annealed at 600 °C and marked as Z600, ZA600, ZC600, and ZCA600 for pure and Al-, Ca-, and Al-Ca-doped electrospun ZnO nanofibers, respectively. PL spectra of the bare and doped ZnO nanofibers are shown in Fig. 25. Peaks A-D and F-peak correspond to defect levels and exciton emission, respectively.

From Fig. 25a, one can conclude that Al, Ca, and Al-Ca doping results in two effects: change of PL intensity and peak shift. When Al is introduced to ZnO matrix, the substitution of Zn by Al occurs. It results to a decrease of F and A-D peaks intensity. In addition, Al forms shallow donor levels in ZnO band gap. These donor levels could participate in photoluminescence, forming donor-acceptor pair. It results in the decrease of emitted photon and a red shift of the PL spectra. Ca doping of ZnO leads to the formation of additional levels in band gap (E-band) and $CaCO_3$ during thermal treatment. This explains the significant decrease of UV emission in ZC600 samples. In ZCA600 samples two competitive effects from Al and Ca dopants keep the position of visible emission non-shifted [48]. It is worth to say that in case of doped metal oxide nanofibers, PL analysis should be combined with other characterization techniques. Correlation between optical and structure properties will be discussed in the next section.

In general, SnO_2, TiO_2, and ZnO are the most common photoluminescence metal oxide nanofibers. However, it is worth to mention about other metal oxide nanofibers which demonstrate photoluminescence at room temperatures.

Kuo et al. (2014) have investigated influence of Sn doping to In_2O_3 photoluminescence. Three emission bands were found in doped In_2O_3 nanofibers, centered at 296–313, 426–455, and 701–718 nm. They correspond to near band edge transitions in In_2O_3 nanofibers, defect levels of Sn, and surface defects, respectively [34]. It was found that an increase of Sn concentration induced blue shift of PL peaks. The mechanism of the PL shift was related to Burstein-Moss effect [34].

Zhou et al. (2016) reported on PL in Ga_2O_3 nanofibers, annealed at different temperatures [49]. Three peaks were observed in Ga_2O_3 nanofibers: 425, 533–550, and 594–634 nm, assigned with structural defects (oxygen vacancies and oxygen interstitials). As deposited Ga_2O_3 nanofibers were amorphous with a high concentration of defects. Annealing of Ga_2O_3 nanofibers at temperatures higher than 450 °C resulted in quenching PL due to a healing of defects [49].

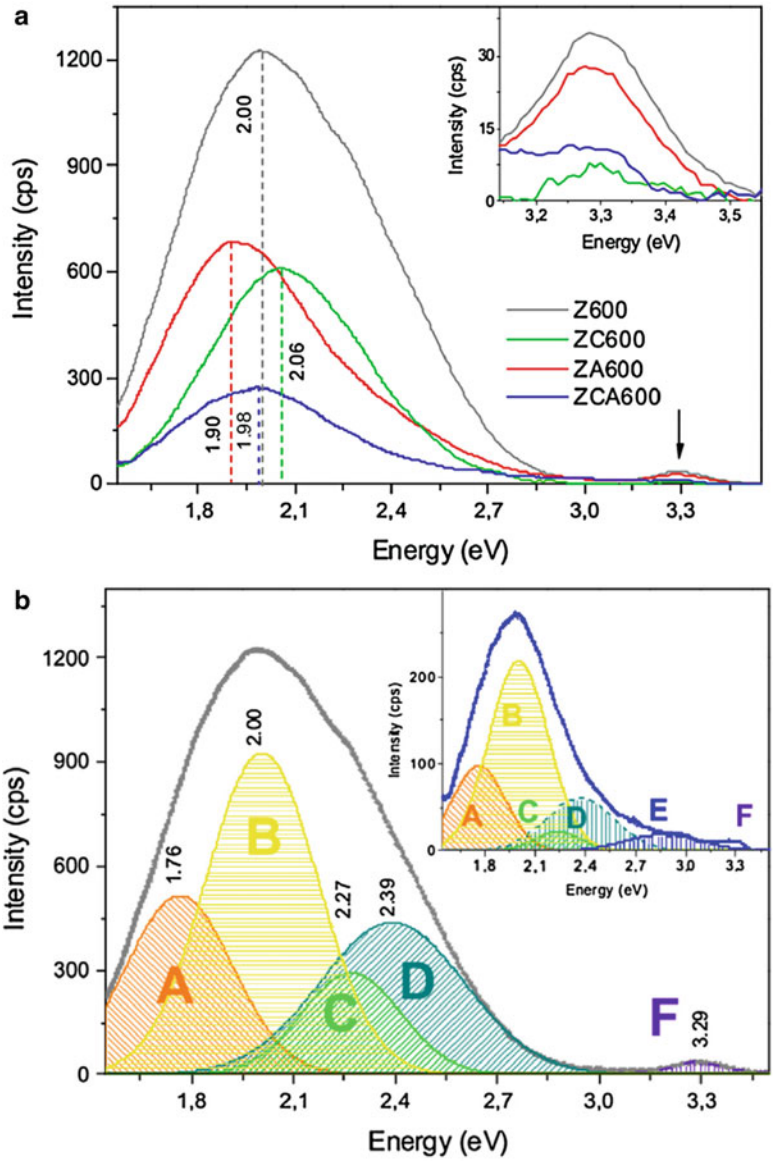

Fig. 25 Photoluminescence spectra of doped ZnO nanofibers: (**a**) full spectra of the samples, inset – region of the NBE emission; (**b**) PL emission contributions in the undoped and co-doped (inset) samples [48]

Ma et al. (2017) reported on PL in Fe-doped WO_3 nanofibers [50]. Two main emission bands were found at 480 and 540 nm, corresponding to band-to-band recombination and defect emission (oxygen vacancies). Fe-doped WO_3 nanofibers showed lower intensities of PL due to charge separation on Fe/WO_3 interface.

Thus, photoluminescence spectroscopy can provide an analysis in polymorphous, doped, and composite materials. It is strongly related to the electronic structure of the metal oxide. PL spectroscopy provides significant changes during variation of structural properties of the metal oxide. In case of several peaks, the PL spectrum requires deconvolution on separate peaks with Gaussian fitting. Interpretation of complex PL spectra requires time, experience, and reference to published results on PL peaks for this type of metal oxide.

Time-Resolved Photoluminescence

Time-resolved photoluminescence is one of the useful methods to evaluate optical and electronic changes due to the structure modification of metal oxide nanofibers. The method is based on excitation of photoluminescence with ultrashort laser pulses (Fig. 26).

Time-resolved photoluminescence spectroscopy requires UV lasers with picosecond or femtosecond pulses and ultrafast photodetectors. Time-resolved photoluminescence can provide information about the lifetime of photoluminescence. This parameter depends on crystallinity of the sample, defect concentration, and dopants.

Ma et al. (2017) investigated time-resolved PL in Fe-doped WO_3 nanofibers (Fig. 27) [50]. The lifetime of WO_3 PL was investigated at different concentrations of Fe dopant. It was shown that PL lifetime increased after Fe doping. It points to charge trapping and charge separation between Fe and WO_3 [50].

Time-resolved spectroscopy can be used to recognize different phases of polymorphous metal oxides [51]. Basic methods of time-resolved spectroscopy for analysis of rutile and anatase phases of TiO_2 are reported.

Das et al. (2009) reported on time-resolved photoluminescence of 1D TiO_2 nanostructures doped with Co [52]. Co-doped TiO_2 nanostructures changed PL spectra due to new defect states related to Co ions. Three decay times were observed, and average decay time was calculated. Co-doping increased the average decay time through the increase of photogenerated electron trapping on defect levels [52].

Thus, time-resolved spectroscopy is a precise method to analyze changes of the electronic structure of metal oxide nanofibers. Although it requires specific tools, the lifetime of photoluminescence can provide information on structure modification and possible applications (photocatalysis for instance) of metal oxide nanofibers.

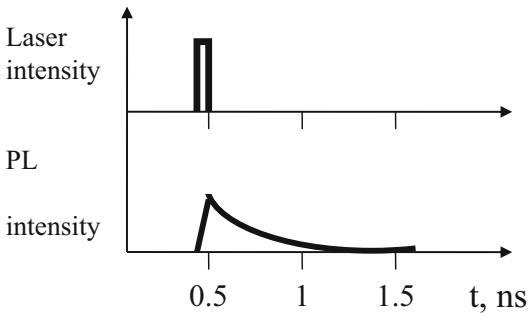

Fig. 26 Scheme of time-resolved photoluminescence

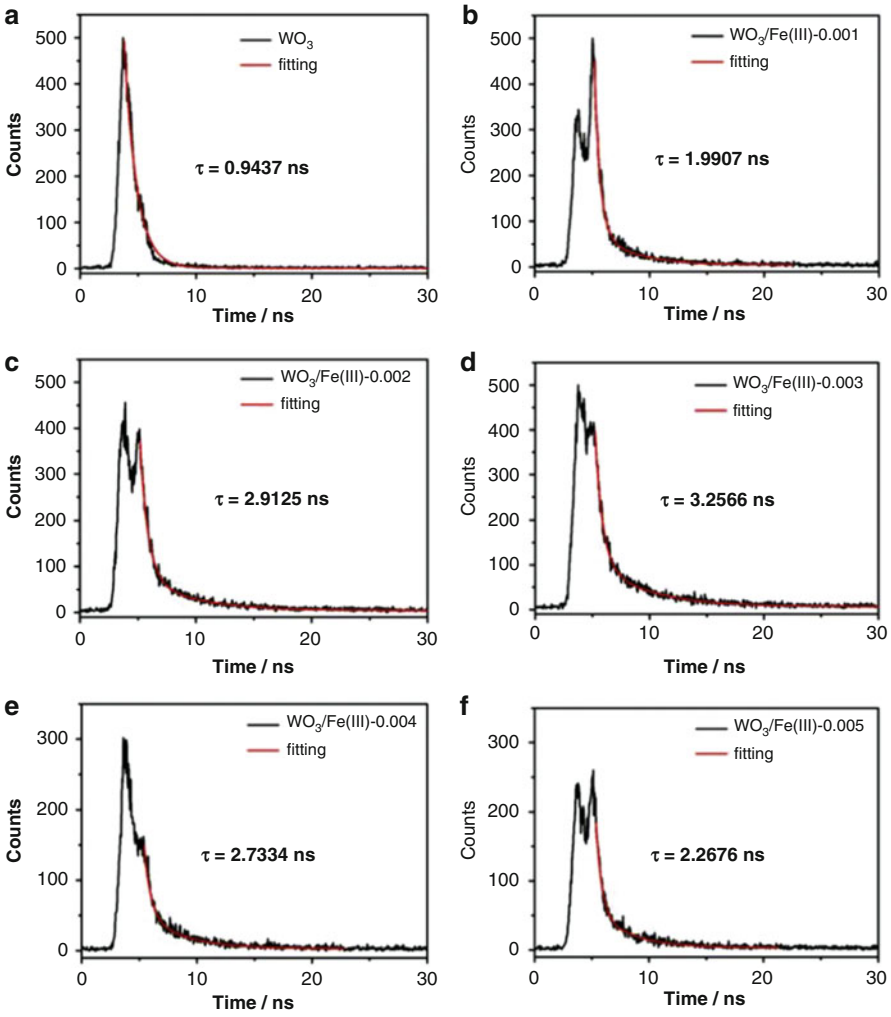

Fig. 27 Time-resolved PL decay curves of WO_3 nanofibers and WO_3/Fe(III) composite nanofibers [52]

Photoluminescence of Core-Shell and Hollow Metal Oxide Nanofibers

One of the novel and prospect research trends in metal oxide nanofibers is a fabrication of core-shell and hollow nanofibers [26, 27, 47]. Organic core is deposited by electrospinning technique. The nanoscale shell coating is formed by atomic layer deposition (ALD) technique [26, 27, 47]. Thermal treatment is preformed to

remove the organic core. Thus, 1D nanostructures with high surface-to-volume aspect ratio can be formed [26, 27, 47].

Viter et al. (2015) demonstrated that ZnO deposited on organic nanofibers demonstrated advanced structural and optical properties [26, 27, 47]. Namely, photoluminescence intensity of the metal oxide nanocoatings increased 1000-fold compared to the same samples, deposited on Si substrates.

Kayaci et al. (2015) investigated the influence of the hollow ZnO nanofiber diameter to optical properties [53]. Two types of polymeric nanofibers were prepared with diameters of 80 and 650 nm. The polymeric nanofibers were coated with ZnO nanolayers, using atomic layer deposition and then annealed at 650 °C to remove the organic core.

Optical properties of core-shell and hollow nanofibers were investigated by photoluminescence spectroscopy (Fig. 28). The thermal treatment resulted in improvement of crystalline structure of the ZnO coatings and reorganization of defect structure. As result, the changes of PL spectra were observed.

One of novel types of core-shell metal oxide nanofibers are metal oxide nanolaminates (multilayered structures), deposited on organic nanofibers. Viter et al. (2016) investigated PL of ZnO/Al_2O_3 nanolaminates, deposited by ALD method on electrospun organic nanofibers [47]. The nanolaminates had different numbers of layers and the bilayer thickness. The total thickness of the coating was kept constant 20 nm for all samples. The bilayer thickness changed from 1 to 20 nm. The obtained PL spectra are shown in Fig. 28. The PL intensity increased due to the increase of defect concentrations with a decrease of bilayer thickness. In addition, Al_2O_3 layers "screened" the internal ZnO layers from the influence of surface charge, formed by adsorbed oxygen [47].

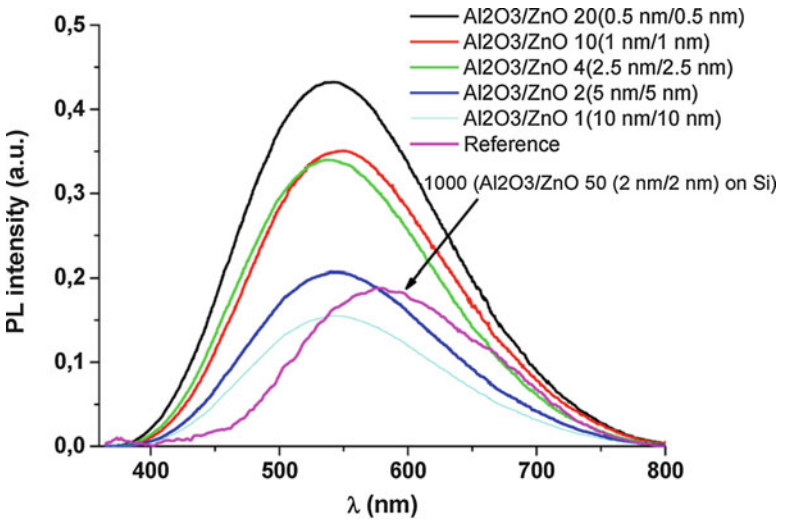

Fig. 28 Room-temperature PL spectra of PAN-Al_2O_3/ZnO nanolaminates with different bilayer thicknesses; Al_2O_3/ZnO nanolaminate 50 (2 × 2 nm) deposited on silicon was added for comparison [47]

Nasr et al. (2016) reported on PL of ZnO nanotubes and ZnO/$ZnAl_2O_4$ multi-co-centric nanotubes [27]. The ZnO and ZnO/Al_2O_3 were deposited on organic nanofibers by ALD method. Annealing at 900 °C has been performed to remove the organic core. As result, ZnO nanotubes showed the highest photoluminescence, whereas the PL intensity significantly decreased with increase of Al_2O_3 phase. It was shown that the PL decrease resulted from phase transitions of ZnO and Al_2O_3 to $ZnAl_2O_4$, induced by temperature [27].

Correlation Between Structural, Electronic, and Optical Properties of Metal Oxide Nanofibers

Optical properties should be analyzed together with electronic and structural properties to avoid explanation errors. For example, Al-doping of ZnO nanofibers and decrease of diameter of the nanofibers will have a similar impact to band gap. Naturally, blue shift is expected in both cases. Therefore, at least XRD and FTIR measurements should be performed in addition to results, obtained by optical method. As example, we can discuss results on correlation of optical and structural properties of ZnO/Al_2O_3 nanolaminates on 1D organic nanofibers, reported in [47]. XPS and FTIR measurements of the samples proved quantum confinement in ZnO/Al_2O_3 nanolaminates due to the decrease in bilayer thickness. No Al-doping effect was observed. The decrease of bilayer thickness resulted in the decrease of grain size and the increase of defect concentration (oxygen vacancies, zinc interstitials, etc.) [47]. Due to that, optical properties (PL) of 1D nanolaminate nanofibers showed a strong increase of emission intensity.

Nasr et al. (2016) made a preliminary XRD analysis of ZnO/Al_2O_3 nanofibers before and after thermal treatment [27]. A new phase of $ZnAl_2O_4$ was identified which assisted the analysis of optical properties and their mechanisms. As $ZnAl_2O_4$ has a much higher band gap than ZnO, a decrease in absorbance was observed due to phase transition and reduction of the ZnO part in the nanocomposite. PL measurements showed a decrease of emission intensity due to phase transitions and charge separation [27].

Thus, the complete study of fundamental properties of metal oxide nanofibers requires comparison and correlation analysis between optical, structural, and electronic properties of the samples.

Optical and Optoelectronic Applications of Metal Oxide Nanofibers

Metal oxide nanofibers have different optoelectronic applications. Due to high surface area and tunable structural and optical properties, the main application of metal oxide nanofibers is photocatalysis for degradation of organic pollutants [27].

However, applications of metal oxides in transparent electrodes [31] and solar cells [38] have been also discussed.

Novel prospect applications of metal oxide nanofibers in UV photodetectors are foreseen [29, 43, 54]. Feng et al. (2011) reported on Al-doped electrospun ZnO nanofibers as optical memory switches. Molina-Mendoza et al. (2016) demonstrated the high photoconductivity of TO_2 electrospun nanofibers. Chayaa et al. (2014) reported on 1D organic core/ZnO shell nanostructures as UV photodetectors. ZnO coating was formed with ALD technique. 1D ZnO UV sensors showed sensitivity 250 times higher than the same ZnO nanolayers on Si substrate.

Viter et al. (2015) reported on the application of 1D organic core/ZnO shell nanostructures as photoluminescence sensors for ethanol vapor detection [15]. Change of PL spectra was detected after ethanol adsorption. Mechanisms of sensitivity were discussed.

Conclusions and Future Prospects

Optical spectroscopy provides a detailed analysis of metal oxide nanofibers. Using Raman, FTIR, PL, and reflectance spectroscopy, one can investigate changes of optical parameters within tuning of structure parameters of metal oxide nanofibers. Optical spectroscopy should be applied together with other methods of structural characterization in order to define correct explanation of the experimental results and physical processes in metal oxide nanofibers.

Future prospects and missing points are related to the following topics:

1. Low-temperature PL measurements of metal oxide nanofibers. There is a limited number of papers in this topic. Some important properties of metal oxide nanofibers (PL activation energy, etc.) can be determined.
2. Photocurrent measurements in visible range. Optically active defects can be investigated, and mechanisms of photoinduced processes in metal oxide nanofibers will get better explanation.
3. Applications of metal oxide nanofibers for optical sensing and biosensing. Due to high surface area and advanced optical properties, metal oxide nanofibers are good candidates for sensing applications. Photoluminescence could be used as measurement method.
4. Photocatalytic applications in visible range. Nanocomposite nanofibers have good prospects for enhancing photocatalytic performance in UV and Vis regions. Band gap tuning through altering different metal oxides is required.

References

1. Smith E, Dent G (2005) Modern Raman spectroscopy – a practical approach. Mod Raman Spectrosc – A Pract Approach. https://doi.org/10.1002/0470011831
2. Iatsunskyi I, Jancelewicz M, Nowaczyk G et al (2015) Atomic layer deposition TiO2 coated porous silicon surface: structural characterization and morphological features. Thin Solid Films 589:303–308. https://doi.org/10.1016/j.tsf.2015.05.056

3. Ferraro JR, Nakamoto K, Brown CW (2003) Introductory Raman spectroscopy: second edition. Introd Raman Spectrosc Second Ed. https://doi.org/10.1016/B978-0-12-254105-6.X5000-8
4. McCreery RL (2000) Raman spectroscopy for chemical analysis. Willey: New York. https://doi.org/10.1002/0471721646
5. Gremlich H-U (2000) Infrared and Raman spectroscopy. Ullmann's Encycl Ind Chem. https://doi.org/10.1002/14356007.b05_429
6. Xie S, Iglesia E, Bell AT (2001) Effects of temperature on the raman spectra and dispersed oxides. J Phys Chem B 105:5144–5152. https://doi.org/10.1021/jp004434s
7. Cuscó R, Alarcón-Lladó E, Ibáñez J et al (2007) Temperature dependence of Raman scattering in ZnO. Phys Rev B 75:1–11. https://doi.org/10.1103/PhysRevB.75.165202
8. Khorasaninejad M, Walia J, Saini SS (2012) Enhanced first-order Raman scattering from arrays of vertical silicon nanowires. Nanotechnology 23:275706. https://doi.org/10.1088/0957-4484/23/27/275706
9. Zhu KR, Zhang MS, Chen Q, Yin Z (2005) Size and phonon-confinement effects on low-frequency Raman mode of anatase TiO2 nanocrystal. Phys Lett Sect Gen Solid State Phys 340:220–227. https://doi.org/10.1016/j.physleta.2005.04.008
10. Meier C, Lüttjohann S, Kravets VG et al (2006) Raman properties of silicon nanoparticles. Phys E Low-Dimensional Syst Nanostruct 32:155–158. https://doi.org/10.1016/j.physe.2005.12.030
11. Iatsunskyi I, Pavlenko M, Viter R et al (2015) Tailoring the structural, optical, and photoluminescence properties of porous silicon/TiO 2 nanostructures. J Phys Chem C 119:7164–7171. https://doi.org/10.1021/acs.jpcc.5b01670
12. Richter H, Wang ZP, Ley L (1981) The one phonon Raman spectrum in microcrystalline silicon. Solid State Commun 39:625–629. https://doi.org/10.1016/0038-1098(81)90337-9
13. Campbell IH, Fauchet PM (1986) The effects of microcrystal size and shape on the one phonon Raman spectra of crystalline semiconductors. Solid State Commun 58:739–741. https://doi.org/10.1016/0038-1098(86)90513-2
14. Iatsunskyi I, Kempiński M, Nowaczyk G et al (2015) Structural and XPS studies of PSi/TiO2 nanocomposites prepared by ALD and Ag-assisted chemical etching. Appl Surf Sci 347:777–783. https://doi.org/10.1016/j.apsusc.2015.04.172
15. Viter R, Chaaya AA, Iatsunskyi I et al (2015) Tuning of ZnO 1D nanostructures by atomic layer deposition and electrospinning for optical gas sensor applications. Nanotechnology 26:105501. https://doi.org/10.1088/0957-4484/26/10/105501
16. Maensiri S, Nuansing W (2006) Thermoelectric oxide NaCo2O4 nanofibers fabricated by electrospinning. Mater Chem Phys 99:104–108. https://doi.org/10.1016/j.matchemphys.2005.10.004
17. Nuansing W, Ninmuang S, Jarernboon W et al (2006) Structural characterization and morphology of electrospun TiO2 nanofibers. Mater Sci Eng B Solid-State Mater Adv Technol 131:147–155. https://doi.org/10.1016/j.mseb.2006.04.030
18. Stuart B (2004) Infrared spectroscopy: fundamentals and applications. Vasa. https://doi.org/10.1007/s13398-014-0173-7.2
19. Doyle WM (1992) Principles and applications of Fourier transform infrared (FTIR) process analysis. Process Control Qual 2:11–41
20. NEAL J (1992) Fourier transform infrared spectroscopy. Encycl Mater Charact 1:416–427. https://doi.org/10.1016/B978-0-08-052360-6.50041-2
21. Ganzoury MA, Allam NK, Nicolet T, All C (2015) Introduction to Fourier transform infrared spectrometry. Renew Sust Energ Rev 50:1–8. https://doi.org/10.1016/j.rser.2015.05.073
22. Imran M, Haider S, Ahmad K et al (2017) Fabrication and characterization of zinc oxide nanofibers for renewable energy applications. Arab J Chem 10:S1067–S1072. https://doi.org/10.1016/j.arabjc.2013.01.013
23. Sharma S, Rani R, Rai R, Natarajan TS (2013) Synthesis and characterization of cuo electrospum nanofiber using poly(vinyl acetate)/Cu(CH3COO)2 annealing method. Adv Mater Lett 4:749–753. https://doi.org/10.5185/amlett.2013.2425

24. Asif SA, Khan S, Asiri AM (2014) Efficient solar photocatalyst based on cobalt oxide/iron oxide composite nanofibers for the detoxification of organic pollutants. Nanoscale Res Lett 9:510. https://doi.org/10.1186/1556-276X-9-510
25. Patil PT, Anwane RS, Kondawar SB (2015) Development of electrospun polyaniline/ZnO composite nanofibers for LPG sensing. Procedia Mater Sci 10:195–204. https://doi.org/10.1016/j.mspro.2015.06.041
26. Viter R, Baleviciute I, Abou Chaaya A et al (2015) Optical properties of ultrathin Al2O3/ZnO nanolaminates. Thin Solid Films 594:96–100
27. Nasr M, Viter R, Eid C et al (2016) Synthesis of novel ZnO/ZnAl2O4 multi co-centric nanotubes and their long-term stability in photocatalytic application. RSC Adv 6:103692–103699
28. Nasr M, Viter R, Eid C et al (2017) Enhanced photocatalytic performance of novel electrospun BN/TiO2 composite nanofibers. New J Chem 41:81–89
29. Feng YY, Hou WT, Zhang XQ et al (2011) Highly sensitive reversible light-driven switches using electrospun porous aluminum-doped zinc oxide nanofibers. J Phys Chem C 115: 3956–3961. https://doi.org/10.1021/jp1117745
30. Chen RQ, Zhu PL, Deng LB et al (2014) Effect of aluminum doping on the growth and optical and electrical properties of ZnO Nanorods. Chem Plus Chem 79:743–750. https://doi.org/10.1002/cplu.201300398
31. Cho Y-Y, Kuo C (2016) Optical and electrical characterization of electrospun Al-doped zinc oxide nanofibers as transparent electrodes. J Mater Chem C 4:7649–7657. https://doi.org/10.1039/C6TC02586B
32. Viter R, Katoch A, Kim SS (2014) Grain size dependent bandgap shift of SnO2 nanofibers. Met Mater Int 20:163–167
33. Nalbandian MJ, Zhang M, Sanchez J et al (2016) Synthesis and optimization of Fe2O3 nanofibers for chromate adsorption from contaminated water sources. Chemosphere 144: 975–981. https://doi.org/10.1016/j.chemosphere.2015.08.056
34. Kuo C-H, Chang P-Y, Chen W-H, Lin S-J (2014) Synthesis of transparent metallic Sn-doped In2O3 nanowires: effects of doping concentration on photoelectric properties. Phys Status Solidi 211:488–493. https://doi.org/10.1002/pssa.201300113
35. Lu N, Shao C, Li X et al (2017) A facile fabrication of nitrogen-doped electrospun In2O3 nanofibers with improved visible-light photocatalytic activity. Appl Surf Sci 391(Part): 668–676. https://doi.org/10.1016/j.apsusc.2016.07.057
36. Chae BW, Amna T, Hassan MS et al (2017) CeO2-Cu2O composite nanofibers: synthesis, characterization photocatalytic and electrochemical application. Adv Powder Technol 28: 230–235. https://doi.org/10.1016/j.apt.2016.09.010
37. Lavanya T, Dutta M, Ramaprabhu S, Satheesh K (2017) Superior photocatalytic performance of graphene wrapped anatase/rutile mixed phase TiO2 nanofibers synthesized by a simple and facile route. J Environ Chem Eng 5:494–503. https://doi.org/10.1016/j.jece.2016.12.025
38. Sahay R, Sundaramurthy J, Kumar PS et al (2012) Synthesis and characterization of CuO nanofibers, and investigation for its suitability as blocking layer in ZnO NPs based dye sensitized solar cell and as photocatalyst in organic dye degradation. J Solid State Chem 186:261–267. https://doi.org/10.1016/j.jssc.2011.12.013
39. Lepcha A, Maccato C, Mettenborger A et al (2015) Electrospun black titania nanofibers: influence of hydrogen plasma-induced disorder on the electronic structure and photo-electrochemical performance. J Phys Chem C 119:18835–18842. https://doi.org/10.1021/acs.jpcc.5b02767
40. Hao YG, Shao XK, Li BX et al (2015) Mesoporous TiO2 nanofibers with controllable Au loadings for catalytic reduction of 4-nitrophenol. Mater Sci Semicond Process 40:621–630. https://doi.org/10.1016/j.mssp.2015.07.026
41. Shen S, Wang X, Chen T et al (2014) Transfer of photoinduced electrons in anatase-rutile TiO2 determined by time-resolved mid-infrared spectroscopy. J Phys Chem C 118:12661–12668. https://doi.org/10.1021/jp502912u

42. George G, Anandhan S (2016) Tuning characteristics of Co3O4 nanofiber mats developed for electrochemical sensing of glucose and H2O2. Thin Solid Films 610:48–57. https://doi.org/10.1016/j.tsf.2016.05.005
43. Chaaya AA, Bechelany M, Balme S, Miele P (2014) ZnO 1D nanostructures designed by combining atomic layer deposition and electrospinning for UV sensor applications. J Mater Chem A 2:20650–20658. https://doi.org/10.1039/C4ta05239k
44. Nasr M, Abou Chaaya A, Abboud N et al (2015) Photoluminescence: a very sensitive tool to detect the presence of anatase in rutile phase electrospun TiO2 nanofibers. Superlattice Microst 77:18–24
45. Ahn K, Pham-Cong D, Choi HS et al (2016) Bandgap-designed TiO2/SnO2 hollow hierarchical nanofibers: synthesis, properties, and their photocatalytic mechanism. Curr Appl Phys 16:251–260. https://doi.org/10.1016/j.cap.2015.12.006
46. Zhang L, Li Y, Zhang Q, Wang H (2014) Well-dispersed Pt nanocrystals on the heterostructured TiO2/SnO2 nanofibers and the enhanced photocatalytic properties. Appl Surf Sci 319:21–28. https://doi.org/10.1016/j.apsusc.2014.07.199
47. Viter R, Iatsunskyi I, Fedorenko V et al (2016) Enhancement of electronic and optical properties of ZnO/Al2O3 nanolaminate coated electrospun nanofibers. J Phys Chem C 120:5124–5132. https://doi.org/10.1021/acs.jpcc.5b12263
48. Santangelo S, Patanè S, Frontera P et al (2017) Effect of calcium- and/or aluminum-incorporation on morphological, structural and photoluminescence properties of electro-spun zinc oxide fibers. Mater Res Bull 92:9–18. https://doi.org/10.1016/j.materresbull.2017.03.062
49. Zhou T, Chen P, Hu S et al (2016) Enhanced yellow luminescence of amorphous Ga2O3 nanofibers with tunable crystallinity. Ceram Int 42:6467–6474. https://doi.org/10.1016/j.ceramint.2015.12.105
50. Ma G, Chen Z, Chen Z et al (2017) Constructing novel WO3/Fe(III) nanofibers photocatalysts with enhanced visible-light-driven photocatalytic activity via interfacial charge transfer effect. Mater Today Energy 3:45–52. https://doi.org/10.1016/j.mtener.2017.02.003
51. Wang XL, Feng ZC, Shi JY et al (2010) Trap states and carrier dynamics of TiO2 studied by photoluminescence spectroscopy under weak excitation condition. Phys Chem Chem Phys 12:7083–7090. https://doi.org/10.1039/b925277k
52. Das K, Sharma SN, Kumar M, De SK (2009) Morphology dependent luminescence properties of Co doped TiO2 nanostructures. J Phys Chem C 113:14783–14792. https://doi.org/10.1021/jp9048956
53. Kayaci F, Vempati S, Ozgit-Akgun C et al (2015) Transformation of polymer-ZnO core-shell nanofibers into ZnO hollow nanofibers: intrinsic defect reorganization in ZnO and its influence on the photocatalysis. Appl Catal B Environ 176–177:646–653. https://doi.org/10.1016/j.apcatb.2015.04.036
54. Molina-Mendoza AJ, Moya A, Frisenda R et al (2016) Highly responsive UV-photodetectors based on single electrospun TiO2 nanofibres. J Mater Chem C 4:10707–10714. https://doi.org/10.1039/c6tc02344d